Available online at www.sciencedirect.com
ScienceDirect
Trans. Nonferrous Met. Soc. China 33(2023) 1373−1384
Transactions of Nonferrous Metals Society of China
www.tnmsc.cn

Effect of AlLi phase on deformation behavior and dynamic recrystallization of Mg−Li alloy during hot compression

Yi GAN[1], Li HU[1], Lai-xin SHI[1], Qiang CHEN[2], Ming-ao LI[1], Lin XIANG[2], Tao ZHOU[1]

1. College of Materials Science and Engineering, Chongqing University of Technology, Chongqing 400054, China;
2. Southwest Technology and Engineering Research Institute, Chongqing 400039, China

Received 12 December 2021; accepted 27 April 2022

Abstract: Hot deformation behavior of Mg−5Li−3Al−2Zn (LAZ532) alloy with AlLi phase was studied by using isothermal hot compression experiments at the deformation temperature of 473−623 K and the strain rate of 0.001−1 s^{-1}. AlLi phase could significantly increase the peak stress of LAZ532 alloy during hot deformation because of its obstructing effect on the movement of dislocation. A relevant strain-compensated Arrhenius constitutive model was constructed to predict the hot deformation behavior of LAZ532 alloy, and the predicted results were in good agreement with experimental ones. The corresponding hot processing maps were established based on the Murty criterion, and the optimal processing domain was located in the range of 538−623 K and 0.001−0.01 s^{-1}. At the high strain rate, AlLi phase was not beneficial for the flow stability and dynamic recrystallization of LAZ532 alloy during hot compression. In addition, deformation temperature would change the nucleation mechanism of the dynamic recrystallization of LAZ532 alloy.

Key words: Mg−Li alloy; AlLi phase; constitutive model; processing map; dynamic recrystallization

1 Introduction

Magnesium−lithium (Mg−Li) alloys have broad application prospect in the aerospace and aviation industries due to their advantages of low density, good damping ability, high specific strength and stiffness [1−4]. Generally speaking, according to the Li content (w_{Li}), Mg−Li alloys are usually divided into three categories, i.e., single α-Mg phase (w_{Li}<5.7%), α-Mg+β-Li phases (5.7% < w_{Li} < 10.3%) and single β-Li phase (w_{Li} > 10.3%) [5−7]. Among them, Mg−Li alloy with single α-Mg phase is the strongest one [8−10]. However, owing to the hexagonal close-packed (HCP) crystal structure, the single α-phase Mg−Li alloys have poor deformation ability at room temperature. Therefore, a complete understanding of the hot deformation behavior of single α-phase Mg−Li alloys is very important for their popularization and application.

In recent years, a few studies have been performed on the hot deformation behavior of single α-phase Mg−Li alloys [11−16]. For example, ASKARIANI and PISHBIN [11] investigated the hot deformation behavior and microstructural evolution of Mg−4Li−1Al alloy by using hot compression and reported that no peak behavior was observed in the flow curves due to the rotation of prismatic plane. LI et al [15] studied the hot deformation mechanism, microstructure evolution and texture types of Mg−5Li−3Al−2Zn alloy and found that the degrees of dynamic recovery (DRV) in deformation grains and dynamic recrystallization (DRX) grain growth increased gradually with the decrease of strain rate. In addition, ZHOU et al [16]

Corresponding author: Lai-xin SHI, Tel: +86-15123376156, E-mail: shilaixin2016@cqut.edu.cn;
Qiang CHEN, Tel: +86-15002389047, E-mail: 2009chenqiang@163.com
DOI: 10.1016/S1003-6326(23)66189-8
1003-6326/© 2023 The Nonferrous Metals Society of China. Published by Elsevier Ltd & Science Press

studied the hot compression deformation behavior and dynamic recrystallization (DRX) of as-cast Mg−4.3Li−4.1Zn−1.4Y alloy with W−$Mg_3Y_2Zn_3$ and $MgZn_2$ phases. They claimed that the size and distribution of the $Mg_3Y_2Zn_3$ and $MgZn_2$ phases would seriously affect the mechanical behavior and DRX process of Mg−Li alloy during hot compression. As indicated, second phases indeed have an important influence on the hot deformation behavior of Mg−Li alloys [14]. On the other hand, AlLi phase, which could provide non-ignorable age hardening and strengthening effects, is a common second phase in the Mg−Li alloys containing a certain amount of Al. However, to our knowledge, little work has so far been carried out on the effect of AlLi second phase on the hot deformation behavior of α-phase Mg−Li alloy.

In this study, we investigated the hot deformation behavior of α-phase Mg−5Li−3Al−2Zn (LAZ532) alloy containing AlLi phase by isothermal hot compression experiments under different deformation temperatures and strain rates. A relevant strain-compensated Arrhenius constitutive model to accurately predict the hot deformation behavior was constructed. The corresponding hot processing maps were also established. In addition, the effects of AlLi phase on the peak stress, processing maps and dynamic recrystallization (DRX) were discussed.

2 Experimental

The single α-phase Mg−Li alloy with chemical composition of Mg−5Li−3Al−2Zn (in wt.%) was applied in the study. To fabricate this alloy, Mg ingots were firstly put into a stainless steel crucible and heated to 993 K. The melting was carried out under the protection of Ar gas. Subsequently, a certain amount of Mg−Al intermediate alloy and Zn ingots were added to the Mg melt and stirred for 5−10 min. A certain amount of pure Li strips wrapped with Al foils were put into the melt and also stirred for 5−10 min. Finally, the melt at the temperature of 963−973 K was poured into a permanent mould to obtain the as-cast Mg−5Li−3Al−2Zn (LAZ532) alloy ingot with a dimension of d50 mm × 145 mm.

Figure 1 shows the schematic diagram of isothermal hot compression experiment. The compressive specimens with a diameter of 8 mm and a height of 12 mm were cut from the cast ingot along the column direction, as shown in Fig. 1. In order to obtain the uniformly distributed AlLi phases, the alloy specimens were homogenized at 623 K for 2 h, and then cooled in water. Microstructure and phase structure of the solution-treated samples were analyzed by using Leica optical microscopy (OM) and X-ray diffraction (XRD) measurement, respectively. Before hot compression, the specimens were heated to the deformation temperature at a rate of 5 K/s, and then kept for 3 min. Afterwards, the specimens were compressed to the true strain of 0.6 via Gleeble−3500 instrument at the selected strain rate (0.001 to 1 s^{-1}) and deformation temperature (473 to 623 K). After hot compression, the compressed specimens were immediately cooled in water to preserve the deformation microstructures. Subsequently, the compressed specimens were cut along the load axis, as shown in Fig. 1, and the microstructures were analyzed by using OM. The radio of etch solution used for the characterization of OM microstructure was 1 mL nitric acid + 1 g oxalic acid + 98 mL distilled water.

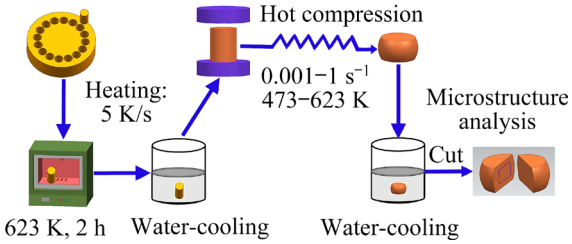

Fig. 1 Schematic diagram of isothermal hot compression experiment

3 Results and discussion

3.1 Microstructure of solution-treated sample before hot compression

Figure 2(a) shows that the equiaxed grains dominate the microstructure of LAZ532 alloy after solution treatment. Moreover, there are some net-like second phases within the matrix, where most of them are distributed at the grain boundaries, and a small part of them are distributed inside the grain interiors. The XRD result indicates that these net-like second phases are AlLi phases, as shown in Fig. 2(b), which is consistent with the result reported by LI et al [10].

3.2 Mechanical behavior during hot compression

Figure 3 shows the true stress–strain curves of LAZ532 alloy containing AlLi phases during hot compression. Obviously, when the deformation temperature is constant, the faster the strain rate is, the higher the peak stress value would be. Correspondingly, when the strain rate is constant, the lower the deformation temperature is, the higher the peak stress would also be. Besides, it is worth noting that, under the same conditions of deformation temperature and strain rate, the value of peak stress of LAZ532 alloy with AlLi phase (see Fig. 3) is usually much higher than that of LAZ532 alloy without AlLi phase [15]. This phenomenon might be attributed to the obstructing effect of the AlLi phase particles with high thermal stability on the movement of dislocation during hot compression of LAZ532 alloy. After the peak stress, the true stress decreases with increasing true strain, suggesting that dynamic softening gradually dominates the hot deformation process. Moreover, some flow stress−strain curves in Fig. 3 are serrated.

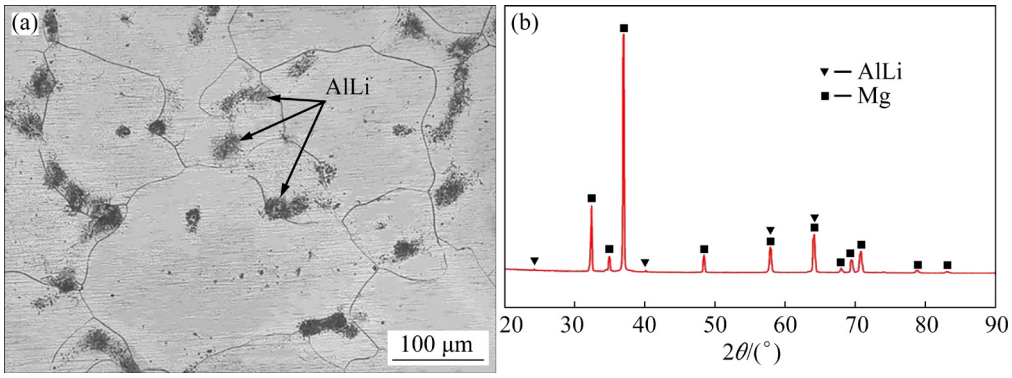

Fig. 2 OM microstructure (a) and XRD pattern (b) of phases for solution-treated sample

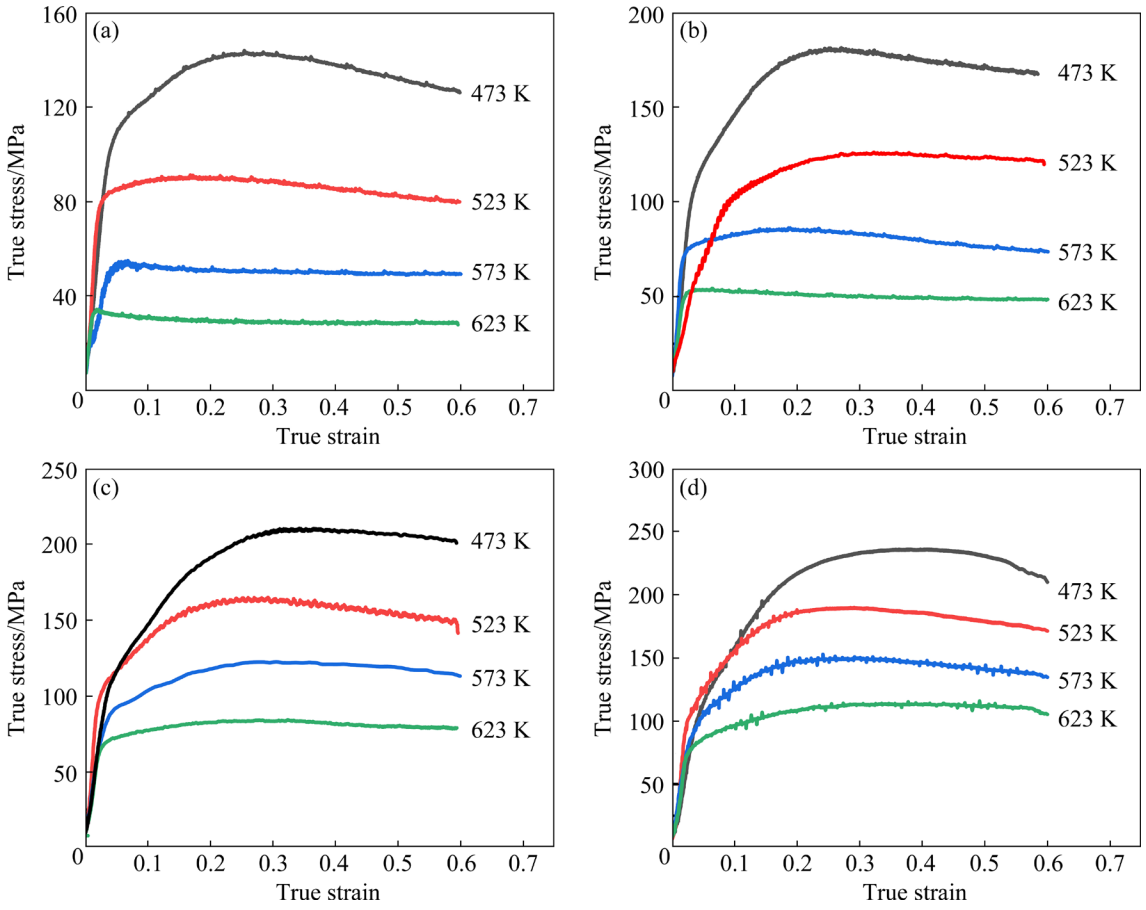

Fig. 3 True stress–strain curves of LAZ532 alloy with AlLi phase under different strain rates: (a) 0.001 s^{-1}; (b) 0.01 s^{-1}; (c) 0.1 s^{-1}; (d) 1 s^{-1}

This issue may be related to the distribution of the second phase and/or the occurrence of discontinuous dynamic recrystallization of metallic materials during hot compression [17,18].

3.3 Construction of constitutive model

It is well known that the deformation behavior of metallic materials during the hot compression is closely related to the deformation condition. In order to describe the relationship among flow stress (σ), deformation temperature (T) and strain rate ($\dot{\varepsilon}$), the traditional Arrhenius-type constitutive model [19] is used in the present study.

Equation (1) can be applied to all deformation conditions [19]:

$$\dot{\varepsilon} = A[\sinh(\alpha\sigma)]^n \exp\left(-\frac{Q}{RT}\right) \quad (1)$$

For deformation conditions at low stress ($\alpha\sigma$<0.8), Eq. (1) could be modified as

$$\dot{\varepsilon} = A_1\sigma^{n_1} \exp\left(-\frac{Q}{RT}\right) \quad (2)$$

For deformation conditions at high stress ($\alpha\sigma$>1.2), Eq. (1) can be expanded as

$$\dot{\varepsilon} = A_2[\exp(\beta\sigma)]\exp\left(-\frac{Q}{RT}\right) \quad (3)$$

where Q is the activation energy of deformation (kJ/mol); R is the molar gas constant (8.314 J/(mol·K)); T is the deformation temperature (K); σ is the flow stress (MPa) at a given strain; A, A_1, A_2, n, n_1, α and β are material constants, with $\alpha=\beta/n_1$ [20].

According to Eqs. (2)−(3) and peak stress (σ_p), the relationships of $\ln\dot{\varepsilon}-\sigma_p$ and $\ln\dot{\varepsilon}-\ln\sigma_p$ can be obtained, as shown in Figs. 4(a) and (c), respectively. The value of β and n_1, which is the average slope of the $\ln\dot{\varepsilon}-\sigma_p$ and $\ln\dot{\varepsilon}-\ln\sigma_p$ fitting lines, can be identified as 0.07391 and 8.73322, respectively. Therefore, the value of α is calculated to be 0.0085.

Taking the natural logarithm on both sides of Eq. (1) and then applying the operation of differentiation, the following equation can be obtained,

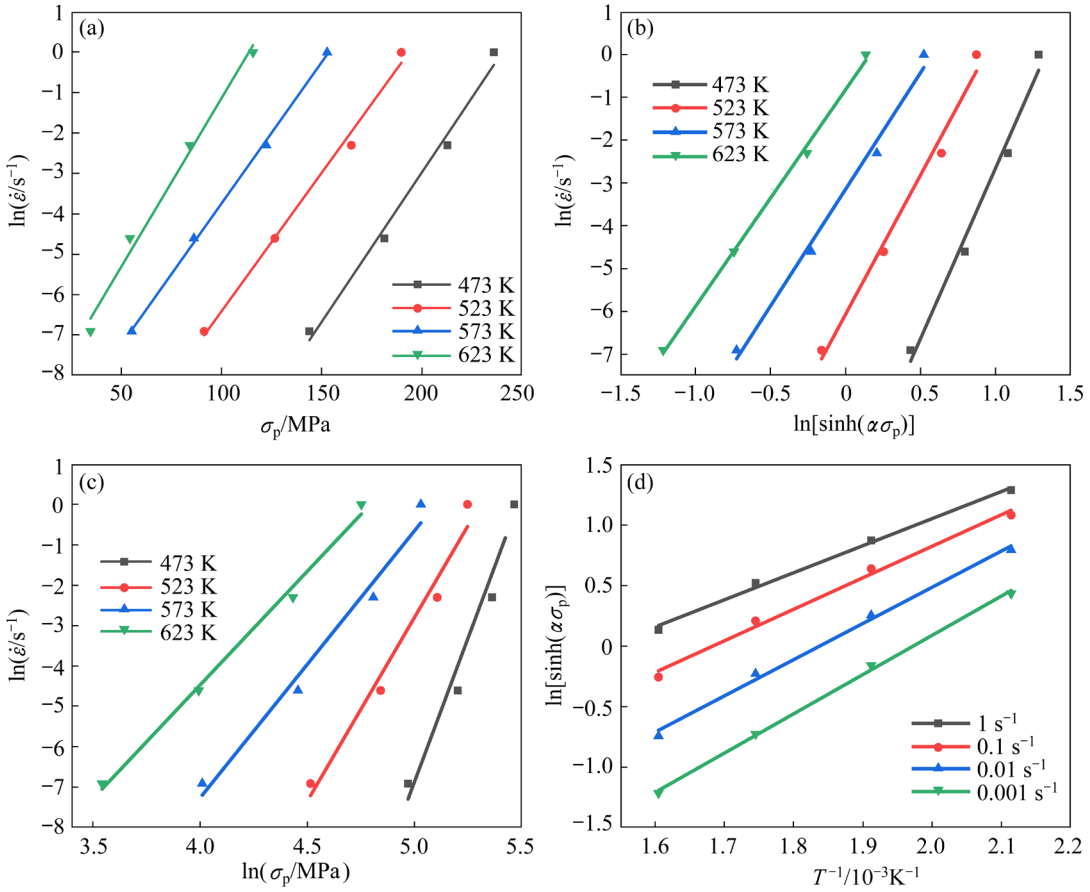

Fig. 4 Linear relationship fitting at peak stress (σ_p): (a) $\ln\dot{\varepsilon}-\sigma_p$; (b) $\ln\dot{\varepsilon}-\ln[\sinh(\alpha\sigma_p)]$; (c) $\ln\dot{\varepsilon}-\ln\sigma_p$; (d) $\ln[\sinh(\alpha\sigma_p)]-T^{-1}$

$$Q = R\left[\frac{\partial \ln \dot{\varepsilon}}{\partial \ln[\sinh(\alpha\sigma)]}\right]_T\left[\frac{\partial \ln[\sinh(\alpha\sigma)]}{\partial(1/T)}\right]_{\dot{\varepsilon}} \quad (4)$$

Based on the values of peak stress (σ_p) in the true stress−strain curves (Fig. 3), the linear relationships of $\ln\dot{\varepsilon} - \ln[\sinh(\alpha\sigma_p)]$ −$\ln[\sinh(\alpha\sigma_p)]$ and $\ln[\sinh(\alpha\sigma_p)]-1/T$ can be obtained, which are shown in Figs. 4(b) and (d), respectively. Thus, the value of n, which is the average slope of $\ln\dot{\varepsilon} - \ln[\sinh(\alpha\sigma_p)]$ fitting lines, can be determined as 6.25304. Afterwards, according to Eq. (4), Figs. 4(b) and 4(d), the value of Q is calculated as about 143.9 kJ/mol for the LAZ532 alloy with AlLi phase.

The influence of strain rate and deformation temperature is usually described by the temperature−compensated deformation rate factor, i.e., Zener-Hollomon parameter (Z) [20,21]:

$$Z = \dot{\varepsilon}\exp\left(\frac{Q}{RT}\right) = A[\sinh(\alpha\sigma)]^n \quad (5)$$

Taking the natural logarithm on both sides of Eq. (5), it extends to the following equation:

$$\ln Z = \ln A + n\ln\sinh(\alpha\sigma) \quad (6)$$

On the basis of the peak stress (σ_p), the relationship between $\ln[\sinh(\alpha\sigma_p)]$ and $\ln Z$ can be indicated in Fig. 5. The correlation coefficient (R^2) of corresponding linear fitting is as high as 0.982. The high value of R^2 indicates that the regression line fits well. Clearly, the value of $\ln A$ can be obtained by calculating the intercept of the $\ln Z$−$\ln[\sinh(\alpha\sigma_p)]$ fitting line. Afterwards, the value of A is calculated as 7.6×10^{11}.

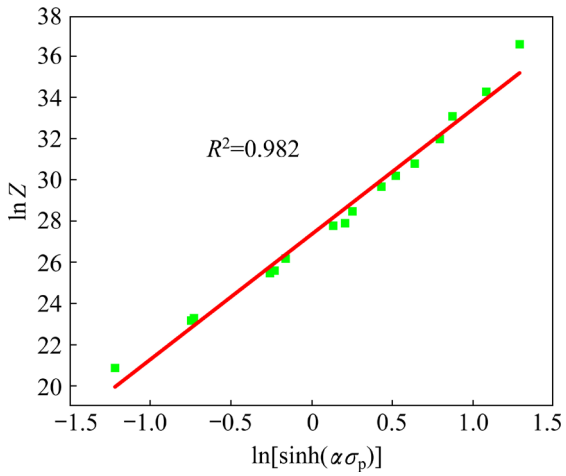

Fig. 5 Relationship between $\ln Z$ and $\ln[\sinh(\alpha\sigma_p)]$

Finally, the constitutive equation (Eq. (7)) of LAZ532 alloy with AlLi phases can be illustrated by substituting the above calculated values of the material parameters (Q, $\ln A$, α and n) into Eq. (1):

$$\dot{\varepsilon}=7.6\times10^{11}[\sinh(0.0085\sigma)^{6.25304}]\exp\left(-\frac{143876}{8.314T}\right) \quad (7)$$

However, it should be pointed out that the values of the main material parameters (α, Q, n and $\ln A$) in the traditional Arrhenius constitutive model (Eq. (1)) are calculated by using the peak stress (σ_p) and they are always fixed, while the effect of plastic strain (ε) is neglected. However, in fact, the plastic strain significantly influences these material parameters (α, Q, n and $\ln A$) during hot deformation [22,23]. Therefore, in this work, in order to predict the hot deformation of the LAZ532 alloy with AlLi phase more accurately via Arrhenius constitutive model, the true stresses corresponding to different true strains (ε) are used for the calculation of these material parameters (α, Q, n and $\ln A$). Multiple values of Q, $\ln A$, α and n under different true strains from 0.05 to 0.55 with an interval 0.05 for the LAZ532 alloy with AlLi phase are obtained by repeating the same calculation process. Table 1 lists the calculated values of material parameters (α, Q, n and $\ln A$).

Afterwards, the relationship between the material parameters (α, Q, n and $\ln A$) and true strain (ε) are expressed as the fifth-order polynomial functions (Eq. (8)) in this study. The specific values of polynomial coefficients are shown in Table 2. Figure 6 shows the fifth-order polynomial fitting

Table 1 Calculated material parameters (α, Q, n and $\ln A$) of LAZ532 alloy containing AlLi phase

ε	α□	Q/(J·mol^{-1})	n	$\ln A$
0.05	0.0119	101840	7.1826	17.8335
0.10	0.0095	168640	9.4381	33.2658
0.15	0.0090	153120	7.2508	29.6460
0.20	0.0087	148170	6.5052	28.4806
0.25	0.0087	146120	6.1869	27.9683
0.30	0.0087	143930	5.9762	27.4745
0.35	0.0088	141340	5.8356	26.8670
0.40	0.0089	140320	5.7597	26.6127
0.45	0.0091	138870	5.5920	26.2882
0.50	0.0092	137670	5.6598	25.9487
0.55	0.0093	137370	5.7404	25.8580

Table 2 Polynomial fitting coefficients of material parameters

α	n	Q/(kJ·mol^{-1})	ln A
α_0=0.0168	n_0=0.4434	Q_0=−0.0580	A_0=−19.4647
α_1=−0.1366	n_1=222.8443	Q_1=4.8690	A_1=1132.6460
α_2=0.8912	n_2=−2040.7354	Q_2=−38.2940	A_2=8928.5684
α_3=−2.8092	n_3=662.5974	Q_3=133.6840	A_3=31250.4582
α_4=4.2821	n_4=−12870.3070	Q_4=−214.9420	A_4=−50381.8390
α_5=−2.5128	n_5=8007.5897	Q_5=129.7440	A_5=30490.8205

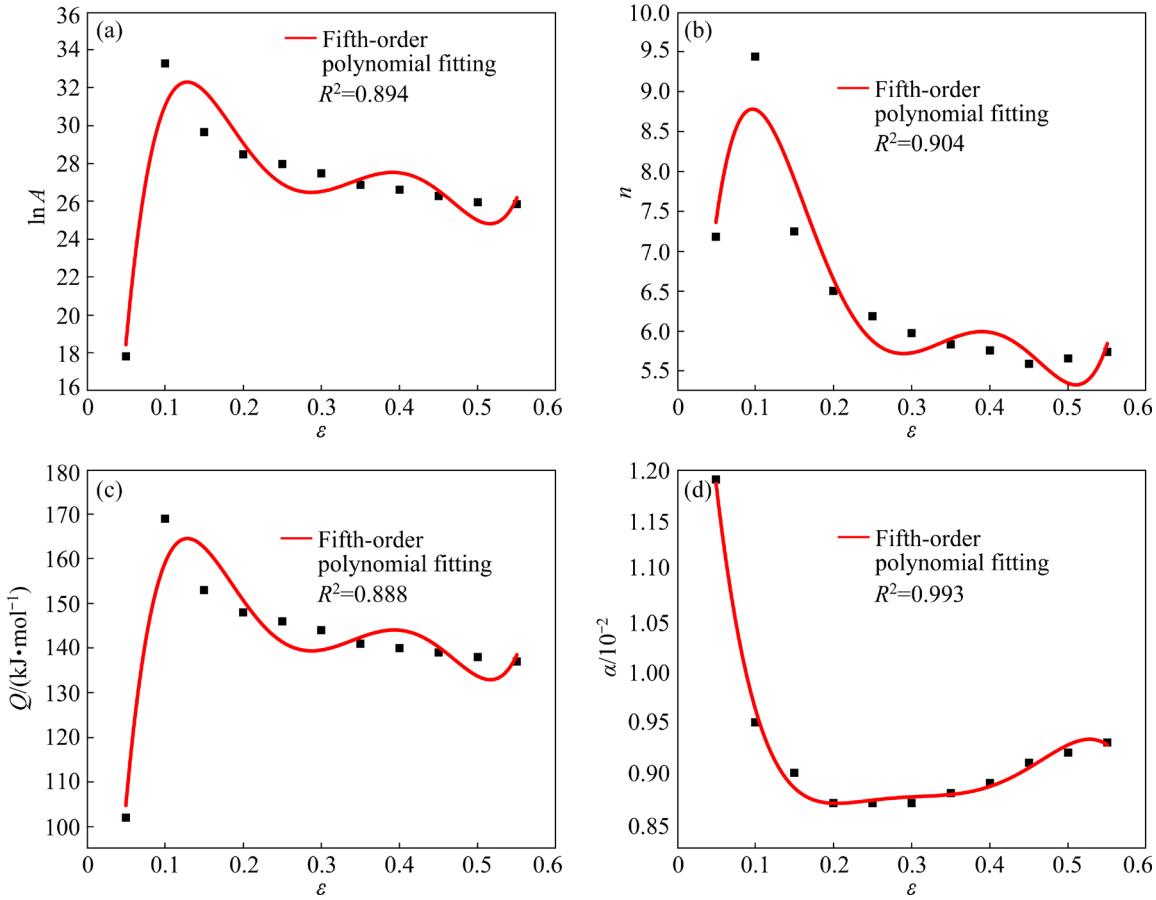

Fig. 6 Relationships between material parameters of ln A (a), n (b), Q (c) and α (d) and ε by using fifth-order polynomial fitting method

results of these material parameters. The corresponding correlation coefficient (R^2) for α, Q, n and ln A is calculated to be about 0.993, 0.888, 0.904 and 0.894, respectively, which indicates a good correlation between the material parameters and the true strain.

$$\begin{cases} \alpha=\alpha_0+\alpha_1\varepsilon+\alpha_2\varepsilon^2+\alpha_3\varepsilon^3+\alpha_4\varepsilon^4+\alpha_5\varepsilon^5 \\ n=n_0+n_1\varepsilon+n_2\varepsilon^2+n_3\varepsilon^3+n_4\varepsilon^4+n_5\varepsilon^5 \\ Q=Q_0+Q_1\varepsilon+Q_2\varepsilon^2+Q_3\varepsilon^3+Q_4\varepsilon^4+Q_5\varepsilon^5 \\ \ln A=A_0+A_1\varepsilon+A_2\varepsilon^2+A_3\varepsilon^3+A_4\varepsilon^4+A_5\varepsilon^5 \end{cases} \quad (8)$$

Finally, using the material parameters (α, Q, n and A) under different strains in Table 1, the flow stress (σ) corresponding to a given strain can be calculated from the following equation:

$$\sigma=\frac{1}{\alpha}\ln\left\{(Z/A)^{1/n}+[(Z/A)^{2/n}+1]^{1/2}\right\} \quad (9)$$

The comparison between the predicted true stress−strain results and the experimental ones are shown in Fig. 7. Obviously, a good consistency can be observed, indicating the validity and necessity of the strain-compensated Arrhenius constitutive

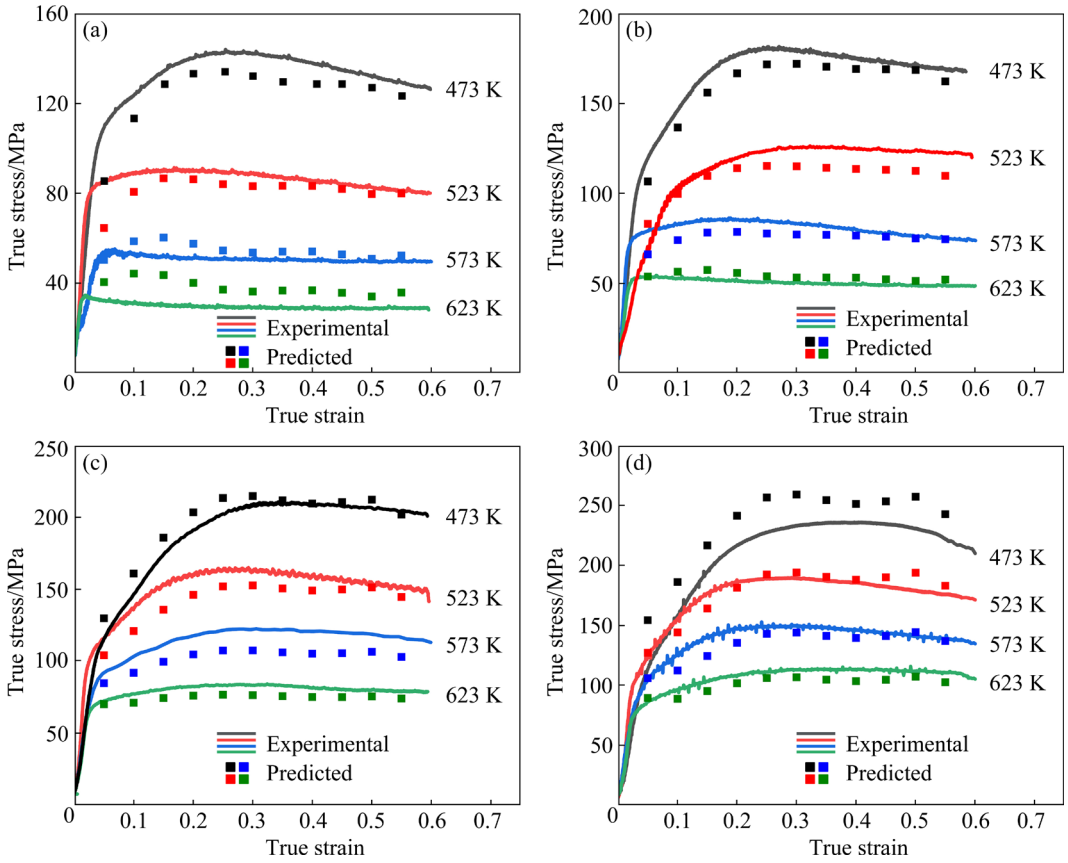

Fig. 7 Experimental and predicted true stress−strain results of LAZ532 alloy with AlLi phase at different strain rates: (a) 0.001 s^{-1}; (b) 0.01 s^{-1}; (c) 0.1 s^{-1}; (d) 1 s^{-1}

model applied to predicting the mechanical behavior of LAZ532 alloy with AlLi phases during hot deformation.

3.4 Construction of processing map

The hot processing map consisting of power dissipation map and instability map has been widely used for investigating the hot deformation behavior of many alloys to optimize the process conditions and control the microstructures [24,25]. Based on dynamic material model (DMM) [26,27], the power dissipation map and instability map can be established by using these obtained true stress–strain curves (Fig. 3). According to the theory of power dissipation, the total energy (P) is composed of the dissipation co-quantity (J) and the dissipation quantity (G). Actually, J is the energy consumed by the evolution of the microstructure in the process of plastic deformation, and G is the energy consumed by the plastic deformation of the material. Therefore, P can be expressed as

$$P=\sigma\dot{\varepsilon}=G+J=\int_0^{\dot{\varepsilon}}\sigma \mathrm{d}\dot{\varepsilon}+\int_0^{\sigma}\dot{\varepsilon}\mathrm{d}\sigma \tag{10}$$

The ratio of J to G is determined by the strain rate sensitivity index (m) under a given temperature and strain condition, namely,

$$m=\frac{\mathrm{d}J}{\mathrm{d}G}=\left[\frac{\partial \ln\sigma}{\partial \ln\dot{\varepsilon}}\right]_{\dot{\varepsilon},T} \tag{11}$$

when m=1, the material is in an ideal linear dissipation state, and the dissipation factor (J) reaches the maximum value (J_{max}):

$$J_{\max}=\frac{1}{2}\sigma\dot{\varepsilon} \tag{12}$$

Furthermore, Murty criterion has great advantages in describing the relationship between flow stress and strain rate, and the criterion is applicable to any kinds of σ versus $\dot{\varepsilon}$ curves [28]. Thus, G content can be calculated from Eq. (13):

$$G=\int_0^{\dot{\varepsilon}}\sigma \mathrm{d}\dot{\varepsilon}=\int_0^{\dot{\varepsilon}_{\min}}\sigma \mathrm{d}\dot{\varepsilon}+\int_{\dot{\varepsilon}_{\min}}^{\dot{\varepsilon}}\sigma \mathrm{d}\dot{\varepsilon}=\left[\frac{\sigma\dot{\varepsilon}}{m+1}\right]_{\dot{\varepsilon}=\dot{\varepsilon}_{\min}}+\int_{\dot{\varepsilon}_{\min}}^{\dot{\varepsilon}}\sigma \mathrm{d}\dot{\varepsilon} \tag{13}$$

where $\dot{\varepsilon}_{\min}$ is the minimum strain rate during hot

deformation. According to the DMM theory, a defined dimensionless parameter (η), which is called as the power dissipation coefficient and represents the proportional relationship between the energy dissipated by the evolution of the microstructure during the material deformation process and the linear dissipated energy, could be expressed as

$$\eta=\frac{J}{J_{\max}}=\frac{P-G}{J_{\max}}=2\left(1-\frac{1}{\sigma\dot{\varepsilon}}\int_0^{\dot{\varepsilon}}\sigma \mathrm{d}\dot{\varepsilon}\right)= 2\left\{1-\left[\left(\frac{\sigma\dot{\varepsilon}}{m+1}\right)_{\dot{\varepsilon}=\dot{\varepsilon}_{\min}}+\int_{\dot{\varepsilon}_{\min}}^{\dot{\varepsilon}}\sigma \mathrm{d}\dot{\varepsilon}\right]\Big/\sigma\dot{\varepsilon}\right\} \quad (14)$$

According to an unstable criterion constructed by MURTY and RAO [29] and the extremum principle of irreversible thermodynamics as applied to large plastic flow, flow instability could be predicted by the following equation:

$$2m<\eta \quad (15)$$

Generally speaking, the evolution of microstructure for the stability zone may involve the dynamic recrystallization, superplasticity, spheroidizing and dynamic recovery with $0<\eta<2m$ and $0<m\leq 1$. However, the typical manifestation of microstructure for the instability zone corresponds to the formation of adiabatic shear bands and/or flow localization, which means $\eta=0$ [28].

Finally, the power dissipation maps are established and the hot processing map could be constructed by superimposing the power dissipation map and instability map. Figure 8 shows the hot processing maps of the LAZ532 alloy with AlLi phase under different true strains. Power dissipation is symbolized by the values on these counter lines and is closely related to the evolution of microstructure. In the hot processing map, the instability zone is represented by the red transparent area, while the stability zone is represented by the non-red transparent area. As indicated in Fig. 8, each hot processing map can be divided into four different regions: a workability region (Domain I), a metastable workability region (Domain II), a transition region (Domain III), and an unsuitable workability region (Domain IV). The instability zones mainly appear under the deformation conditions of high strain rate or low deformation temperature, which clearly indicates that high strain rate or low deformation temperature is unsuitable for the hot deformation of LAZ532 alloy with AlLi phases. Moreover, it is worth noting that the instability zone occurs under the deformation condition of high strain rate and high deformation temperature (1 s^{-1}, 573−623 K) for the LAZ532 alloy with AlLi phase (see Fig. (8)), but it is not

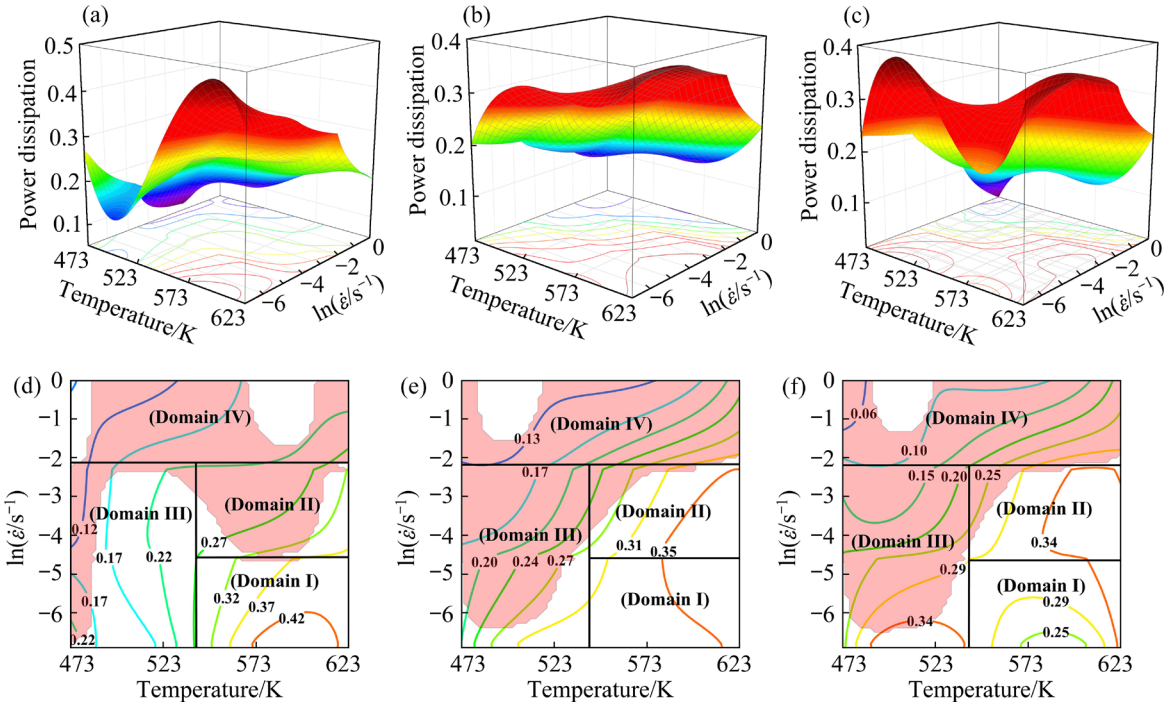

Fig. 8 Power dissipation maps (a, b, c) and corresponding hot processing maps (d, e, f) of LAZ532 alloy with AlLi phase during isothermal hot compression at different true strains: (a, d) 0.2; (b, e) 0.4; (c, f) 0.6

observed for the LAZ532 alloy without the AlLi phase [15]. Accordingly, it is reasonable to deduce that AlLi phase could significantly influence the distribution of instability zones in the hot processing map and is unfavorable for the flow stability of the LAZ532 alloy during hot deformation at high strain rate. On the other hand, in the Domain I with the deformation temperature in the range of 538−623 K and the strain rate in the range of 0.001−0.01 s^{-1}, the instability zone is absence, and meanwhile, the power dissipation efficiency is also high enough. Accordingly, Domain I can be selected as the optimal processing region for the LAZ532 alloy with AlLi phase.

3.5 Microstructure characteristics under different deformation conditions

Figures 9(a−d) show the microstructure characteristics of the LAZ532 alloy with AlLi phase deformed to the true strain of 0.6 at a given

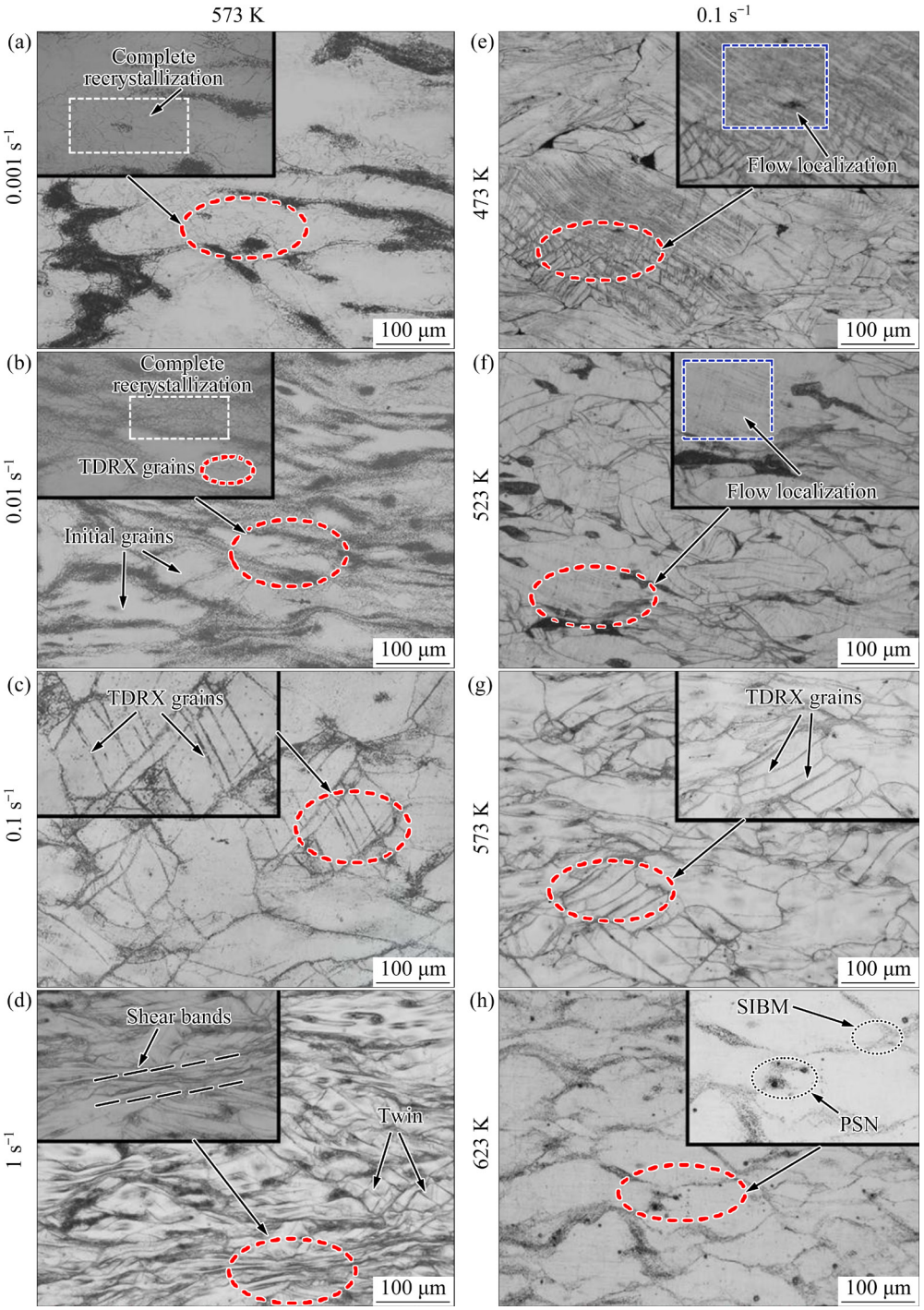

Fig. 9 Microstructure characteristics of LAZ532 alloy with AlLi phase during hot compression: (a−d) 0.001−1 s^{-1}, 573 K; (e−h) 473−623 K, 0.1 s^{-1}

deformation temperature of 573 K and different strain rates. When the strain rate (1 s^{-1}) is relatively high, only a few twins can be observed in the deformed gains, as shown in Fig. 9(d). Moreover, there are also some shear bands in the deformed microstructure, which might lead to the flow instability of the LAZ532 alloy with AlLi phase during hot compression at this deformation condition (573 K, 1 s^{-1}) (see Fig. 8). However, under the same deformation condition (573 K, 1 s^{-1}), for the LAZ532 alloy without AlLi phase during hot compression, the dynamic recrystallization (DRX) occurs while the shear band is not observed [15]. The results clearly demonstrate that AlLi phase is unfavorable for the occurrence of DRX and the flow stability of the LAZ532 alloy deformed at high strain rate. When the strain rate decreases to 0.1 s^{-1}, as shown in Fig. 9(c), twins are also observed and many fine DRX grains are distributed at the twin boundaries. This nucleation mechanism of dynamic recrystallization induced by twins is called as twin dynamic recrystallization (TDRX) nucleation [30]. With the further decrease of strain rate to 0.01 s^{-1}, the DRX grains might have more time to nucleate and grow at the twin boundaries. Accordingly, the size of TDRX grains increases significantly and the trend of complete recrystallization becomes more evident, as shown in Fig. 9(b). When the strain rate decreases to 0.001 s^{-1}, as shown in Fig. 9(a), many complete DRX grains can be observed, which actually corresponds to the flow stability of the LAZ532 alloy with AlLi phase during hot compression at this deformation condition (573 K, 0.001 s^{-1}) (see Fig. 8). As indicated, low strain rate is beneficial for the occurrence of DRX and the flow stability of the LAZ532 alloy with AlLi phase during hot deformation.

Figures 9(e−h) show the microstructure characteristics of LAZ532 alloy with AlLi phase deformed to the true strain of 0.6 at a constant strain rate of 0.1 s^{-1} and different deformation temperatures. Under the lower deformation temperatures of 473−523 K, it can be found that flow localization occurs within the deformed microstructure, as shown in Figs. 9(e, f), which might result in the flow instability of the LAZ532 alloy with AlLi phase during hot compression (see Fig. 8). As the deformation temperature increases to 573 K, twin dynamic recrystallization (TDRX) gains can be observed (see Fig. 9(g)). When the deformation temperature further increases to 623 K, as shown in Fig. 9(h), some DRX grains can be observed near the boundaries of deformed grains. This mechanism of dynamic recrystallization nucleation is called as the strain-induced boundary migration (SIBM) nucleation [31]. In addition, as mentioned above, AlLi phase with high thermal stability serves as the major second phase in the LAZ532 alloy used in this study, which can effectively obstruct the movement of dislocations. Consequently, during hot compression, numerous dislocations might be accumulated near the AlLi phase particles, which can contribute to a large increase in the deformation stored energy and thus stimulate the nucleation of the dynamic recrystallization (DRX) grains (see Fig. 9(h)). This nucleation mechanism of DRX caused by the AlLi second phase particles is called as particle stimulated nucleation (PSN) [31]. Obviously, the above results indicate that, for the LAZ532 alloy with AlLi phase during hot compression, the high deformation temperature is benefit to the nucleation of DRX grains according to the SIBM and PSN mechanisms.

4 Conclusions

(1) The AlLi phase can significantly increase the peak stress of the LAZ532 alloy during hot compression. Moreover, according to the experimental true stress–strain data, a relevant strain-compensated Arrhenius constitutive model was constructed to accurately predict the hot deformation behavior of LAZ532 alloy with AlLi phase. The predicted true stress–strain results have good consistency with the experimental ones.

(2) The corresponding hot processing maps of LAZ532 alloy with AlLi phase were constructed based on the Murty criterion. At high strain rate, AlLi phase is unfavorable for the flow stability of the LAZ532 alloy during hot compression. The optimal processing region could be identified as the Domain I with the deformation temperature in the range of 538−623 K and the strain rate in the range of 0.001−0.01 s^{-1}.

(3) For the LAZ532 alloy with AlLi phase during hot compression, as the deformation temperature increased, the nucleation mechanism of dynamic recrystallization (DRX) would transform from the twin dynamic recrystallization (TDRX)

nucleation to the strain-induced boundary migration (SIBM) nucleation and the particle stimulated nucleation (PSN). However, at high strain rate, AlLi phase was not beneficial for the occurrence of DRX in the LAZ532 alloy during hot compression.

Acknowledgments

This study was funded by the National Natural Science Foundation of China (Nos. 51822509, 51701034), the Scientific and Technological Research Program of Chongqing Municipal Education Commission, China (Nos. KJQN201801137, KJQN201901106), and the Basic and Advanced Research Project of CQ CSTC, China (No. cstc2018jcyjAX0035).

References

[1] CHEN Xiao-yang, ZHANG Yang, CONG Meng-qi, LU Ya-lin, LI Xiao-ping. Effect of Sn content on microstructure and tensile properties of as-cast and as-extruded Mg8Li3Al(1,2,3)Sn alloys [J]. Transactions of Nonferrous Metals Society of China, 2020, 30: 2079−2089.

[2] ZHAO Zi-long, SUN Zi-wei, LIANG Wei, WANG Yi-de, BIAN Li-ping. Influence of Al and Si additions on the microstructure and mechanical properties of Mg−4Li alloys [J]. Materials Science and Engineering A, 2017, 702: 206−217.

[3] LI Chuan-qiang, TONG Zhi-pei, HE Yi-bin, HUANG Huai-pei, DONG Yong, ZHANG Peng. Comparison on corrosion resistance and surface film of pure Mg and Mg−14Li alloy [J]. Transactions of Nonferrous Metals Society of China, 2020, 30: 2413−2423.

[4] PARK G H, KIM J T, PARK H J, KIM Y S, JEONG H J, LEE N, SEO Y, SUH J Y, SON H T, WANG W M, PARK J M, KIM K B. Development of lightweight Mg−Li−Al alloys with high specific strength [J]. Journal of Alloys and Compounds, 2016, 680: 116−120.

[5] TANG Yan, LE Qing-chi, JIA Wei-tao, LIU Xu-an, CUI Jian-zhong. Influences of warm rolling and annealing processes on microstructure and mechanical properties of three parent structures containing Mg−Li alloys [J]. Materials Science and Engineering A, 2018, 711: 1−11.

[6] TANG Yan, LE Qi-chi, MISRA R D K, SU Guan-qiao, CUI Jian-zhong. Influence of extruding temperature and heat treatment process on microstructure and mechanical properties of three structures containing Mg−Li alloy bars [J]. Materials Science and Engineering A, 2018, 712: 266−280.

[7] BECERRA A, PEKGULERYUZ M. Effects of lithium, indium, and zinc on the lattice parameters of magnesium [J]. Journal of Materials Research, 2008, 23: 3379−3386.

[8] LI Xiao-qiang, CHENG Chun-long, LE Qing-chi, BAO Lei, JIN Ping-wang, WANG Ping, REN Liang, WANG Hang, ZHOU Xiong, HU Cheng-lu. Investigation of Portevin–Le Chatelier effect in rolled α-phase Mg−Li alloy during tensile and compressive deformation [J]. Journal of Materials Science and Technology, 2020, 52: 152−161.

[9] ZHANG Cheng, WU Liang, ZHAO Zi-long, XIE Zi-hui, HUANG Guang-sheng, LIU Lei, JIANG Bin, ATRENS A, PAN Fu-sheng. Effect of Li content on microstructure and mechanical property of Mg−xLi−3(Al−Si) alloys [J]. Transactions of Nonferrous Metals Society of China, 2019, 29: 2506−2513.

[10] LI Ji-qiang, QU Zhi-kun, WU Rui-zhi, ZHANG Mi-lin. Effects of Cu addition on the microstructure and hardness of Mg–5Li–3Al–2Zn alloy [J]. Materials Science and Engineering A, 2010, 527: 2780−2783.

[11] ASKARIANI S A, PISHBIN S H. Hot deformation behavior of Mg−4Li−1Al alloy via hot compression tests [J]. Journal of Alloys and Compounds, 2016, 688: 1058−1065.

[12] ZHOU Yu-cheng, CHEN Zhao-yun, JI Jing-han, SUN Zhi-jie. Optimization of hot deformation parameters and constitutive analysis for as-cast Mg−5Li−3Zn−0.3Y alloy using processing maps [J]. Journal of Materials Engineering and Performance, 2018, 27: 4606−4615.

[13] ZHOU Yu-cheng, CHEN Zhao-yun, JI Jing-han, SUN Zhi-jie. Dynamic nano precipitation behavior of as-cast Mg−4Li−4Zn−Y alloy during high temperature deformation [J]. Materials Science and Engineering A, 2017, 707: 110−117.

[14] LI Yi, GUAN Yan-jin, ZHAI Ji-qiang, LIN Jun. Hot deformation behavior of LA43M Mg−Li alloy via hot compression tests [J]. Journal of Materials Engineering and Performance, 2019, 28: 7768−7781.

[15] LI Xiao-qiang, REN Liang, LE Qing-chi, JIN Pei-peng, CHENG Chun-long, WANG Tong, WANG Ping, ZHOU Xiong, CHEN Xing-rui, LI Dan-dan. The hot deformation behavior, microstructure evolution and texture types of as-cast Mg–Li alloy [J]. Journal of Alloys and Compounds, 2020, 831: 154868.

[16] ZHOU Yu-cheng, CHEN Zhao-yun, JI Jing-han, SUN Zhi-jie. Effects of second phases on deformation behavior and dynamic recrystallization of as-cast Mg−4.3Li−4.1Zn−1.4Y alloy during hot compression [J]. Journal of Alloys and Compounds, 2019, 770: 540−548.

[17] XUE Yong, ZHANG Zhi-min, LU Guang, XIE Zhi-ping, YANG Yong-biao, CUI Ya. Study on flow stress model and processing map of homogenized Mg−Gd−Y−Zn−Zr alloy during thermomechanical processes [J]. Journal of Materials Engineering and Performance, 2015, 24: 964−971.

[18] MWEMBELA A, KONOPLEVA E B, MCQUEEN H J. Microstructural development in Mg alloy AZ31 during hot working [J]. Scripta Materialia, 1997, 37: 1789−1795.

[19] CAO Fu-rong, YIN Bin, LIU Si-yuan, SHI Lu, WANG Shun-cheng, WEN Jing-lin. Microstructural evolution, flow stress and constitutive modeling of Al−1.88Mg−0.18Sc−0.084Er alloy during hot compression [J]. Transactions of Nonferrous Metals Society of China, 2021, 31: 53−73.

[20] YUAN Cheng-hao, LIU Bin, LIU Yu-xi, LIU Yong. Processing map and hot deformation behavior of Ta-particle reinforced TiAl composite [J]. Transactions of Nonferrous Metals Society of China, 2020, 30: 657−667.

[21] BAREZBAN M H, MIRZADEH H, ROUMINA R, MAHMUDI R. Constitutive analysis of wrought Mg-Gd

magnesium alloys during hot compression at elevated temperatures [J]. Journal of Alloys and Compounds, 2019, 791: 1200−1206.

[22] BAO Cheng-li, ZHOU Tao, SHI Lai-xin, LI Ming-ao, HU Li, YANG Ming-bo, CHEN Qiang. Hot deformation behavior and constitutive analysis of as-extruded Mg−6Zn−5Ca−3Ce alloy fabricated by rapid solidification [J]. Metals, 2021, 11: 480.

[23] WANG Yong-jian, PENG Jian, ZHONG Li-ping, PAN Fu-sheng. Modeling and application of constitutive model considering the compensation of strain during hot deformation [J]. Journal of Alloys and Compounds, 2016, 681: 455−470.

[24] YANG Qing-bo, DENG Yan-jun, YANG Mou, ZHANG Zhi-qing, LI Wei-guo, LIU Qing. Effect of Al_3Zr particles on hot-compression behavior and processing map for Al−Cu−Li based alloys at elevated temperatures [J]. Transactions of Nonferrous Metals Society of China, 2020, 30: 872−882.

[25] GUO Yu-hang, XUANYUAN Yao-dong, LY Xuan-nam, YANG Sen. Hot deformation behaviors of the Mg−3Sn−2Al−1Zn alloy: investigation on its constitutive equation, processing map, and microstructure [J]. Materials, 2020, 13: 312.

[26] WANG Xu, LI Zhou, XIAO Zhu, QIU Wen-ting. Microstructure evolution and hot deformation behavior of Cu−3Ti−0.1Zr alloy with ultra-high strength [J]. Transactions of Nonferrous Metals Society of China, 2020, 30: 2737−2748.

[27] MORAKABATI M, HAJARI A. Hot working behavior of near alpha titanium alloy analyzed by mechanical testing and processing map [J]. Transactions of Nonferrous Metals Society of China, 2020, 30: 1560−1573.

[28] MA Xiong, ZENG Wei-dong, XU Bin, SUN Yu, XUE Chen, HAN Yuan-fei. Characterization of the hot deformation behavior of a Ti−22Al−25Nb alloy using processing maps based on the Murty criterion [J]. Intermetallics, 2012, 20: 1−7.

[29] MURTY S V S N, RAO B N. On the development of instability criteria during hotworking with reference to IN 718 [J]. Materials Science and Engineering A, 1998, 254: 76−82.

[30] XIAO H C, JIANG S N, TANG B, HAO W H, GAO Y H, CHEN Z Y, LIU C M. Hot deformation and dynamic recrystallization behaviors of Mg−Gd−Y−Zr alloy [J]. Materials Science and Engineering A, 2015, 628: 311−318.

[31] ZHU N Y, SUN C Y, LI Y L, QIAN L Y, HU S Y, CAI Y, FENG Y H. Modeling discontinuous dynamic recrystallization containing second phase particles in magnesium alloys utilizing phase field method [J]. Computational Materials Science, 2021, 200: 110858.

AlLi 相对 Mg−Li 合金热压缩变形行为和动态再结晶的影响

甘 翼[1]，胡 励[1]，时来鑫[1]，陈 强[2]，李明骜[1]，向 林[2]，周 涛[1]

1. 重庆理工大学 材料科学与工程学院，重庆 400054；
2. 西南工程技术研究所，重庆 400039

摘 要：采用等温热压缩实验研究含有 AlLi 相的 Mg−5Li−3Al−2Zn(LAZ532)合金的热变形行为；变形温度和应变速率范围分别为 473~623 K 和 0.001~1 s^{-1}。LAZ532 合金热变形过程中 AlLi 相能够阻碍位错运动，从而显著提高合金的峰值应力值。为精确预测 LAZ532 合金的热变形行为，构建相应的应变补偿 Arrhenius 本构模型，预测结果与实验结果吻合良好。基于 Murty 准则，建立相应的热加工图，合理的加工区域在 538~623 K 和 0.001~0.01 s^{-1} 范围内。在高应变速率变形条件下，AlLi 相不利于 LAZ532 合金在热压缩过程中的流动稳定性和动态再结晶。此外，变形温度会改变 LAZ532 合金的动态再结晶形核机制。

关键词：Mg−Li 合金；AlLi 相；本构模型；加工图；动态再结晶

(Edited by Xiang-qun LI)